Title
East Asian Rainbands and Associated Circulation over the Tibetan Plateau Region

Journal
Journal of Climate, 35(11)

ISSN
0894-8755

Authors
Liu, Jiabin
Fung, Inez Y
Chiang, John CH

Publication Date
2022-06-01

DOI
10.1175/jcli-d-21-0569.1

Peer reviewed

East Asian Rainbands and Associated Circulation over the Tibetan Plateau Region

Jiabin Liu*

Department of Earth and Planetary Science, University of California, Berkeley, Berkeley, California

Inez Y. Fung

Department of Earth and Planetary Science, University of California, Berkeley, Berkeley, California

John C. H. Chiang

Department of Geography, University of California, Berkeley, Berkeley, California

**Corresponding author*: Jiabin Liu, jiabin@berkeley.edu

ABSTRACT

Rainbands that migrate northward from spring to summer are persistent features of the East Asian summer monsoon. This study employs a machine learning algorithm to identify individual East Asian rainbands from May to August in the 6-hourly ERA-interim reanalysis product, and captures rainband events during these months for the period 1979-2018. The median duration of rainband events at any location in East Asia is 12 hours, and the centroids of these rainbands move northward continuously from approximately 28°N in late May to approximately 33°N in July, instead of making jumps between quasi-stationary periods. While the length and overall area of the rainbands grow monotonically from May to June, the intensity of the rainfall within the rainband dips slightly in early June before it peaks in late June.

We find that extratropical northerly winds on all pressure levels over East China are the most important anomalous flow accompanying the rainband events. The anomalous northerlies augment climatological background northerlies in bringing low moist static energy air and thus generate the front associated with the rainband. Persistent lower tropospheric southerly winds bring in moisture that feeds the rainband and are enhanced a few days prior to rainband events, but are not directly tied to the actual rainband formation. The background northerlies could originate as part of the Rossby waves resulting from the jet stream interaction with the Tibetan Plateau. Meanwhile, the ageostrophic circulation in the jet entrance region peaks in May and weakens in June and July and does not prove to be critical to the formation of the rainbands.

1. Introduction

One of the most recognizable features of the East Asian climate is the Meiyu-Baiu-Changma rainy season, part of the East Asian Summer Monsoon. During this rainy period, certain places in East China, Korea, and Japan experience persistent rainfall that typically forms an elongated pattern. Analysis using 5-day averaged precipitation suggests that "rain belts" may be semi-stationary and undergo a stepwise northward transition from spring to summer in climatology, but can have pauses and jumps in a given year (Ding and Chan (2005)). The analysis also shows that rain belts with the heaviest precipitation typically consist of meso-scale disturbances along weather fronts (Ding and Chan (2005)). Day et al. (2018) used a simple algorithm to identify narrow elongated precipitation features in 57 years of East Asian daily precipitation at 25 km, and found that East China receives about 60% of its annual precipitation from these frontal rainbands.

Banded precipitation occurs in many places around the world; these rainbands range from tens to thousands of kilometers in length and may have different characteristics and dynamic origins. They include mesoscale structures embedded in extratropical cyclones (Houze et al. (1976)), snow bands downwind of large water bodies due to the lake-effect (Niziol et al. (1995)), and orographic precipitation anchored over mountain ranges, such as those found in Japan (Yoshizaki et al. (2000)), the Southern German Alps (Hagen (1992)), and east of the Rockies in the United States (Fairman et al. (2016)). However, most orographic precipitation has its maximum either at the peak (for small mountains) or on the windward slope (for large mountains), as the most prominent mechanism of the precipitation here is the lofting of moist air parcels upslope (Roe (2005)). Precipitation fronts can also form downwind if the mountains are large enough. Two processes contribute to the formation of these fronts: the convergence downstream after the flow goes around the obstacle, and the uplifting created by the advection of heat from the top of the mountain (Barrett et al. (2015)).

Orographic precipitation bands are particularly interesting because they form typically downwind of large mountains and because their quasi-stationary nature leads to the accumulation of large amounts of rainfall in a more predictable pattern than other synoptic weather systems.

Hypotheses about the characteristics of the East Asian rainbands involve the Pacific Ocean, the topography in East Asia, and the large-scale circulation. The intensity of rainfall in the Meiyu-Baiu-Changma rainbands is typically tied to variations in sea surface temperatures of the adjacent seas as well as to aerosols and other aspects of climate change(e.g. Lau et al. (2006); Liang and He (2008); Chen et al. (2013)). Intense Meiyu precipitation is hypothesized to be associated with ENSO, as El Niño-like conditions and anomalous anticyclones in the western North Pacific are found to precede periods of enhanced Meiyu rainfall (Wang and Li (2004)). Wu et al. (2015) hypothesized that sensible heating over the Tibetan Plateau in the summer drives a large scale circulation that intensifies the East Asian summer monsoon.

Moisture sources are thought to be central to the formation of the rainbands. Climatologically, the southerly and south-easterly low-level winds transport water vapor to the extra-tropics and the mid-latitude. Xu et al. (2001) and Wu et al. (2018) attributed the Meiyu onset to the intensification and northward movement of the western Pacific subtropical high pressure system, which transports increasingly humid air northwestward from ocean to the East Asian continent from spring to summer. The intensification and movement of the western Pacific subtropical high are in turn related to convection in the ITCZ and the Bay of Bengal (Zhou et al. (2004)). Some of this moisture is deposited in southwestern China, and some continues to move northward to fuel the East Asian banded precipitation. This continual moisture supply is seen as a part of the coupling of the South Asian and East Asian precipitation in July and August (Day et al. (2015)). While dynamic effects anchor the position of the rainbands, the supply of moisture can determine the precipitation amount to a large degree. The southerly moisture transport that fuels the rainbands have also been attributed to the dynamical effect of the Tibetan Plateau, generating Rossby Waves in the downstream and therefore the southerlies over East Asia (Son et al. (2019)). The seasonal shift of the impinging westerly wind in turn controls the seasonal evolution of this southerly flow as well (Son et al. (2020)).

The jet stream and the Tibetan Plateau also play critical roles in the formation, movement, and termination of East Asian banded precipitation. The jet stream is at its maximum speed in the jet entrance region over the west Pacific, where the East Asian rainbands are located. The meridional temperature gradient increases here, so the jet stream accelerates to maintain thermal wind balance. This acceleration is achieved by a transverse circulation, similar to the Hadley cell, maintaining angular momentum conservation (Chapter 6, Holton and Hakim (2013)). This transverse circulation has an ascending branch south of the jet stream, leading to precipitation (Liang and Wang (1998)). The jet entrance region, in turn, results primarily from extratropical heating (e.g. Held et al. (2002); Chang (2009)). Zonally asymmetric extratropical heating could be produced by the jet stream interacting with the Tibetan Plateau (Molnar et al. (2010)). The westerly flow impinging on the Tibetan Plateau is deflected to flow around the plateau, leading to northerly winds and convergence downstream. The East Asian rainband season terminates when the jet stream moves north of the latitudinal range of the Tibetan Plateau in summer and is no longer interacting with the topography (Kong and Chiang (2020)). In addition, interaction with local convection also plays a role in the strengthening of the jet stream here, such as that with the heating from Baiu rainfall (Matsumura et al. (2016)).

In this study, we focus on a detailed characterization of the East Asian rainbands and an analysis of the associated atmospheric circulation, using 6-hourly fields from ERA-Interim from 1979-2018 (Dee et al. (2011)). Unlike previous studies that focus on Meiyu (over China) or Baiu (over Japan), we do not distinguish precipitation over land from that over the ocean, nor do we separate it by country. In fact, historically, Meiyu and Baiu refer to a particular time period when certain locations experience persistent rainfall, rather than to a large-scale pattern in weather or climate. The subject of this study is the west-east elongated and continuous pattern of precipitation and its associated dynamics. This frontal pattern contributes to a significant portion of precipitation during Meiyu and Baiu, but is by no means equivalent to these terms describing the total rainfall. Indeed, Day et al. (2018) found that frontal and non-frontal rainfall over China during Meiyu season exhibit different decadal trends and hence have different dynamical controls.

In the following sections, we confine our analysis to the mechanical aspects of the circulation that contribute to the seasonal migration of the rainbands, and do not address here the companion thermodynamic and hydrodynamic aspects of the rainbands. Section 2 describes novel methods using image processing techniques and deep neural networks to identify individual rainbands in the precipitation data. The climatology of the East Asian rainbands is presented in Section 3. Section 4 examines the atmospheric circulation accompanying the rainbands to diagnose processes for the formation and seasonal migration of the rainbands.

2. Data and Method

a. Data

This work uses 6-hourly total precipitation, wind (U, V), temperature, and specific humidity fields for 1979 to 2018 from the European Centre for Medium-Range Weather Forecasts (ECMWF) Interim Re-Analysis (ERA-Interim) products (Dee et al. (2011)). The data have a resolution of $0.75° \times 0.75°$ and 37 pressure levels extending from 1000 hPa to 1 hPa. While previous studies have discovered some discrepancies between precipitation amounts in reanalysis products and rain gauge measurements (Sun et al. (2018)), we have found good comparison between the ERA-Interim precipitation patterns and those in rain-gauge data in East Asia. Furthermore, the reanalysis product provides precipitation over the ocean and facilitates the study of the full extent of rainbands. Using the full suite of data from the same reanalysis product analysis also enables us to examine the atmospheric circulation accompanying the rainbands.

b. Method of Detection

We applied a machine learning procedure to identify, on a 6-hourly time scale, the latitudinal and longitudinal extents of the west-east extending rainbands occurring over East Asia. This procedure used a combination of image processing techniques, manual labeling, and deep neural networks.

The analysis focuses on the domain of the East Asian rainbands, from 20°N to 45°N and 110°E to 145°E, encompassing the Middle and Lower Yangtze Plain to the west and the east coast of Japan to the east, the southern border of mainland China to the south, and the Chinese-Russian border to the north. We have experimented with slightly different domains, including the domain of the East Asian Summer Monsoon defined by Wang (2002) (20°N to 45°N and 110°E to 140°E), but the results (not all shown) are qualitatively similar and do not change our conclusion.

We started from the 6-hourly total precipitation in ERA-interim from January 1979 to December 2018 and applied the rainband detection methods (discussed below) to the entire record. In later sections, the presentation focuses on May to August, the rainy season in East Asia and when banded precipitation is most likely to occur.

Our machine learning detection method involves three steps: (1) definition of connected patterns of 6-hourly precipitation using an initial threshold of precipitation greater than 10 mm/day and pattern longer than 10 degrees in longitude; (2) manual examination of every connected pattern in a subset of randomly-selected patterns each month to identify a distinct feature of a long and narrow banded precipitation band from large patches of precipitation; and (3) a convolutional neural network model trained on the outcome of the first two steps (see Figure 1) and applied to the remainder of the dataset. This way we not only articulate a clear requirement for the rainbands but also eliminate false positives that meet the threshold requirements. As an example, a rainfall pattern around 28°N and extending eastward from 110°E in Figure 2(a) (red contour is 10 mm/day in total precipitation) would be identified as a positive rainband candidate as the result of the three-step identification process. In contrast, a large cluster of unorganized rainfall over the East China Sea (Figure 2(b)) might have been identified as a rainband by the thresholds in the first step, but visual inspection and the deep neural network is able to tell that this pattern is different from the narrow and linear thin and clean rainbands that this work seeks to identify. Below we elaborate on each step of the detection method.

The first step selects candidates for rainbands by finding continuous areas where the 6-hourly total precipitation is greater than 10 mm/day. Among these areas, we choose the one with the longest longitudinal extent. This way, we convert the precipitation map into a binary representation: grid boxes with rainfall greater than 10 mm/day are labeled as 1 (hereafter "1-grids"), and grid boxes with less or no rainfall are labeled as 0 (hereafter "0-grids"). The results of detection are qualitatively not sensitive to the exact choice of the threshold.

On the binary image from the previous step, we then label all connected components with 4 connectivity, meaning we find all the areas where the 1-grid shares at least one side with another 1-grid. We assign each connected area with a unique group ID. Two 1-grids that touch only at a vertex are not considered to be connected and therefore do not belong to the same group. The labeling of the connected components in digital images is one of the most fundamental operations in pattern recognition and computer vision; it has become efficient and easy to implement and proves to be useful in tracking objects in many types of analysis (He et al. (2009)). The labeling serves as a foundation for automating the recognition of complex patterns in climate and many other fields.

The labeling of connected components is not sufficient for our purpose of identifying rainbands. There is no guarantee that the longest connected area in the longitudinal direction has the structure of an elongated narrow band. It could be mesoscale storm systems that are wide in the north-south direction as well or has a twisted shape, and would not represent a real rainband. We could have limited the north-south extent of this connected area or simply limited its size, but this limiting approach would miss some true positives without increasing the accuracy much. Furthermore, the labeling of connected components is not robust to small gaps; a long rainband with a one-pixel gap in the middle may not be recognized as a band, leading to false negatives in rainband recognition. While the approach to find connected components gives an approximate account of the rainbands, further steps are needed to make sure the rainbands are correctly detected, so that the analysis on circulations associated with the rainbands can be meaningful.

Manual labeling of rainbands could have been a solution to the aforementioned problems, but labeling 58,400 (4x365x40) maps of precipitation for the 40 years of data is not only labor-intensive but would also be subject to inconsistencies when there is a change in personnel engaged in labeling or when an updated or extended record is available. Convolutional neural networks are powerful tools for image classification and require images of the positive class (rainfall maps with manually identified rainbands) and images of the negative class (rainfall maps without any rainband identified). Here, we trained a convolutional neural network to identify rainbands in the remainder of the rainfall maps with a relatively small number of labeled images (approximately 500 for each class).

To ensure that the training data - the approximately 1000 labeled rainfall maps - are representative, we carried out stratified random sampling of the labeled groups of connected components from the first step above. The manual labeling seeks thin, straight, and long (in the west-east direction) strips of continuous precipitation isolated from other patches of rainfall. The negative class was sampled for all 12 months of each year, and the positive class was sampled mostly in spring and summer when rainbands are prevalent. This way we made sure that the model can recognize a negative class of different patterns; a rainy day without rainbands in the summer, for example, looks different from a rainy day without rainbands in the winter; the former can see a lot of unorganized convective rainfall or cyclonic disturbances, while the latter may be light rains from stratiform clouds. The advantage of manual labeling after the first automated connected-component labeling lies in the significant savings in labor.

Our convolutional neural network consists of two hidden layers, with a max-pooling of stride 2 and 16 nodes. The inputs are binary images found in step 1 where pixels with "1" represent total precipitation more than 10 mm/day, and pixels with "0" represent precipitation less than that or no precipitation at all. Each image is classified as "positive", namely with at least one rainband candidate, or "negative", namely without a rainband candidate. The images represent the area between 20°N to 45°N and 110°E to 145°E and are of size 34 x 46 in pixels. We choose one of the simplest neural networks possible without any hyperparameter tuning to avoid overfitting. A comprehensive strategy in choosing the parameters for neural networks is beyond the scope of this study, but it is a fairly simple task to recognize a horizontal narrow band in a picture. The model trained with 10 epochs reaches 95% accuracy in both training and testing.

This model was then applied to identify rainbands in the rest of the dataset. When the neural network identifies a rainband, we returned to the result of connected-component labeling to find the exact location of the longest rainband: its extent in all four directions, the total amount of rainfall in the band, and the location of the centroid of the rainfall. This hierarchical approach to identify the rainband strikes a balance between accurate recognition and easy automation; it can be readily adapted to other datasets or to identify other patterns in climate.

3. Climatology of the East Asian Rainband

Using ERA-interim 6-hourly total precipitation fields from 1979 to 2018, we found, in the domain of 20°N to 45°N, 110°E to 145°E, 503 snapshots with rainbands in May, 1047 in June, 473 in July, and 166 in August. With 40 years of records and 4 snapshots per day, the numbers translate to 3.1 days in May, 6.5 days in June, 3.0 days in July, and 1.0 days in August with rainbands on average. June is the peak season for Meiyu rainbands, and May and July see similar numbers of bands, about half of that in June. In August the occurrence of Meiyu rainbands decreases further. Day et al. (2018) found a similar peak of the occurrence of frontal precipitation in the Meiyu season (mid-June to mid-July), but with a higher rate of occurrence (60% for the Meiyu season) because their identification thresholds of 10 mm/day and 5 degrees longitude were applied to daily precipitation accumulation rather than to a 6-hourly snapshot.

Figure 3 shows the climatology of the latitude of the rainband centroids and the longitudinal extent, whereas Figure 4 shows the eastern and western boundaries of the rainbands. Here we define "snapshot climatologies" as the 40-year average of the rainband statistics for each 6-hour of each day (e.g. 12Z on May 1). In May, the East Asian rainbands are located around 28°N, corresponding to the southern Chinese province Guangxi and Guangdong, and also northern Taiwan; the rainbands are already north of the South China Sea. In fact, the South China Sea sees much rainfall throughout early spring to the beginning of fall, but the rainfall is sporadic and not organized into elongated bands. Therefore the intense rainfall over the South China Sea, while part of the Asian monsoon,should not be seen as part of the evolution of the East Asian rainbands because it is convective rather than frontal.

As shown in Figure 4, the longitudinal extent of the rainbands lengthens from May and peaks in late June, before it decreases again and stabilizes in August. The rainbands undergo this change by first extending the eastern boundary from 132°E to 136°E from May to June, and then extending the western boundary from 120°E to 115°E from June to July. The two boundaries then retreat to around 133°E and 120°E in August. This east-west expansion of banded rainfall has not received as much attention in previous literature as the north-south movement, but nevertheless helps characterize the evolution of the rainband.

The elongated banded rainfall moves northward from 28°N in mid-May to around 32°N in mid-July. Previous literature, using climatologies of 5-day rainfall amounts, documents this northward movement as stepwise, with three stationary stages separated by two abrupt jumps(e.g. Ding and Chan (2005); Wang (2002)). Our 6-hourly snapshot climatology shows instead that the northward movement is steady and smooth, and the rainbands do not linger in preferred locations as previously described in pentad climatologies of total rainfall. Our snapshot climatology does not rule out the possibility that there are interludes of intense non-frontal quasi-stationary (within 5 days) mesoscale precipitation systems at some locations, or that the rainbands could indeed stall some seasons. Interannual variations in summer precipitation over China has a typical "South Flood North Drought" pattern, with heavy rains of the Yangtze River basin (29°N to 32°N) (e.g. Day et al. (2015)) and may be attributed to enhanced frequencies of the rainbands (Day et al. (2018)). Ding and Chan (2005) pointed out the East Asian summer monsoon originates from the South China Sea (Indochina Peninsula), then jumps to the Yangtze River Basin, before it finally reaches North China and the Korean Peninsula. As part of the East Asian summer monsoon system, the rainbands we identified shows the preferred latitude to be beyond 26° N in climatology. This indicates that the first stage of the summer monsoon in the south might not be in the form of organized, banded precipitation. Our study also shows while the rainbands do sometimes penetrate past Beijing (approximately 40° N) and reach northeast China and Korea, their strengths diminish and their lengths shrink. As a result, rainbands no longer stand out as the prominent rainfall feature over East Asia around this time. Also, this northward penetration occurs in mid to late summer, when the South Asian monsoon is at its peak and the South China Sea experiences intense rainstorms, so these southern components of precipitation dominate over the dwindling Meiyu in the discussion of rainfall over China. Indeed, in Figure 3, the rainbands retreat southward and disperse from mid-July to August. Overall, the strong and coherent banded features of precipitation this study focuses on are not directly equivalent to the full East Asian summer monsoon system documented in previous studies, but are rather one component of it.

The relative strength between the East Asian rainbands and total precipitation is further illustrated in Figure 5. Here we composited the maps of total precipitation over this broader region of East Asia (20°N to 45°N, 110°E to 145°E) at times when an East Asian rainband is identified over the search domain. The composite includes non-banded precipitation that occur at the same time as the rainbands. From May to July, the rainbands stand out as the only feature in the entire domain of Asia. The centroid of the rainbands shifts slightly north from May around 28°N to 30°N in June, and to 32°N in July. In August, there are fewer rainbands than the previous months, the rainband-composites anomalies do not stand out above the August climatology (less than 5 mm/day), and the bands are more spread out and further north of their July location, consistent with their northward seasonal progression. We note that the August band of intense rainfall in south China align with the Nanling (Southern) Mountains, which block August typhoon rains from penetrating inland.

The patterns of rainband precipitation in each month appear more prominently once the background rainfall is removed, i.e. with the subtraction of the monthly mean total precipitation from the monthly precipitation composites at times when rainbands are identified (Figure 6). The anomalies capture the peak rainfall intensities in the rainband. As shown in Figure 6, the rainband-composite precipitation anomalies also illustrate behaviors less documented in previous studies: on top of the climatological precipitation, the positive rainband precipitation anomalies move eastward from May to August. In May, the western tip of the rainband anomalies penetrate southwest China to the foothill of the Yunnan-Guizhou Plateau. In June, while the rainband composites grow longer as shown in Figure 5, the rainband anomalies retreat to the downstream of the Yangtze River basin in East China. This period is also what is commonly recognized as Meiyu because it affects this densely populated region in China and is well observed. In June and July, the rainbands are the dominant contributors to total precipitation, and so the rainband-composite anomalies are thus lower than earlier in the season. In July the positive anomalies still cover the Yangtze River basin and Southern Japan, while the negative anomalies grow over Western Pacific, suggesting rainfall over this region starts to become prominent in the climatology. In August, the heaviest rainbands precipitation anomalies appear in the Korean Peninsula, with weaker patterns spanning east China, the sea of Japan, north China, and the southern bit of Russia. Meanwhile, the strong rainfall over Western Pacific dominates the climatology and shows up as negative anomalies.

While the length and latitudinal position of the rainbands change monotonically from May to June, the intensity of the precipitation within the rainbands tells a slightly different story, as shown in Figure 7. Intensity is defined here as the total amount of precipitation in the identified rainband divided by the number of grids in the rainband. This intensity reaches a local maximum in mid-May before it dips slightly at the beginning of June, and then increases again towards the end of June, when the rainbands are longest. The rainfall within rainbands declines in intensity in July and stabilizes in August, when the rainbands are more dispersed, suggesting the dynamic process of the rainbands might have experienced changes from previous months. The rainbands also make the biggest contribution to the total amount of precipitation over East Asia in June, and this contribution declines in July and August (figure not shown). This different trend from that of the length or the position of the rainbands indicates that the intensity of the rainbands is likely also influenced by a different dynamic process than the size or location of them. In July and August, ample moisture appears over East Asia along with the rising temperature, and this moisture fuels the precipitation over South China and the Pacific Ocean that covers a much larger area than the rainbands do. Even with the same frontal condition, moisture supply can significantly impact how much precipitation a rainband event gets, but will likely not affect whether or where it happens.

The prolonged duration of total precipitation is one of the most prominent features in Meiyu and Baiu season. We calculated rainband duration as the number of continuous snapshots where a rainband is present, multiplied by the time interval between two snapshots (6 hours). An average event lasts for 16 hours, and a median event lasts for 12 hours. As shown in Figure 8, the duration of the rainband is the shortest in August, the longest in June, and seldom last longer than 48 hours. Rainbands lasting longer than 48 hours happen mostly in June, albeit with a small fraction of 7 percent. Indeed, the longest event lasting 228 hours was in June 1998. Thus, the stalling of rain belts found in previous analysis of pentad climatologies is likely due to multiple rainbands occurring within 5 days in a large gridbox as well as synoptic disturbances along the front rather than frontal rainbands analyzed here. Notice that a rainband event is not equivalent to Meiyu or Baiu rainfall, in that only a large-scale precipitation pattern will be characterized as a rainband, but a localized convective rainfall in a city or region will be seen as Meiyu. Therefore, Meiyu season could last weeks, while a long rainband event only last a few days.

4. Atmospheric Circulation Associated with the East Asian Rainbands

The East Asian precipitation in spring and early summer are frontal banded precipitation with origin in large-scale convergence of cold dry northerly winds and warm moist southerly winds, unlike the rain in the mid-to-late summer that is mostly convective. Previous studies hypothesized that the upper-tropospheric jet stream and the subtropical high-pressure system over Western Pacific play a role partly because, similar to the rainbands, they migrate northward from spring to summer (e.g. Ding and Chan (2005)). Sampe and Xie (2010) also argued that the jet stream is responsible for mid-tropospheric advection of heat from the top of the Tibetan Plateau eastward, thus creating the banded precipitation by uplifting the air.

In this section, we analyze the composites of the atmospheric circulation accompanying rainband events to show that the northerly wind over East China is the strongest anomalous signature when rainband events occur. This northerly determines the latitudinal position of the fronts, and therefore of the rainbands; when the northerly weakens and eventually disappears, the rainband season also ends. The seasonally-varying position and strength of this northerly is a result of the seasonal northward migration of the upstream westerlies relative to the Plateau, and the resulting interaction between them. Here we composite atmospheric circulation variables (e.g. precipitation, northerlies) of 6-hourly time slots within a month or season when rainbands are detected, and refer to them as rainband-composites. Departures of rainband-composites from monthly or seasonal climatologies are referred to as rainband-composite anomalies.

The climatological monthly mean 500-hPa winds (Figure 9, right column) show that the northward migration of the westerly jet stream across the Tibetan Plateau from spring to summer is accompanied by a weakening of the northerly winds over East China. Note that even though the jet core is at a higher level around 200-hPa, it still has its signature at 500-hPa, and the 500-hPa winds illustrate the interaction of the flow with topography more clearly than the 200-hPa winds and are the most relevant for the climate of East Asia. In June, the jet stream is near the northern reaches of the Tibetan Plateau and begins to weaken. In July and August, the core of the jet stream is completely north of the plateau, and the monthly-mean winds are mostly zonally oriented.

The rainband-composite of the 500-hPa wind fields (Figure 9, left column) yields a slightly different picture. While both the monthly mean wind fields and the rainband-composite winds show signatures of the subtropical jet stream, a northerly component over East China is always present for the rainband-positive composites, but not discernible in the monthly mean for July and August.

The difference is the clearest in the rainband-composite anomalies of the monthly mean 500-hPa winds (Figure 10). In all four months, the anomalies show easterlies and northerlies over northern China and Russia, and westerly and southerly over the sea of Japan. This cyclonic circulation anomaly is strong in May, July, and August, but slightly weaker in June. In June, this cyclonic flow, especially the northerly wind over East China, is already evident in the monthly-mean field, and so is only slightly strengthened on the days with rainbands. This finding agrees with Ninomiya and Muraki (1986), which observed a similar cyclonic circulation associated with Baiu and Meiyu from May to July in 1979. As shown with the overlay of the anomaly of moist static energy (MSE), the anomalous northerlies are associated with the presence of anomalously low moist static energy air into this region, implying that the northerlies bring about the low MSE air, which then generates the front.

In the following, we focus on the rainband front over East China, as its seasonal migration is well-documented in the rain-gauge data. The convergence and the front are more easily observed in the cross-section of the climatological meridional circulation. Rainbands are located where the meridional gradient of the moist static energy is steepest, around 30° N on average May-August. Throughout the season when rainbands are prominent (from May 1^{st} to Aug 31^{st}), a pattern of convergence is evident between 110°E and 120°E, with northerly and southerly winds dominant northward and southward, respectively, of 30°N (Figure 11). We chose this range of longitude as it is the region with the strongest influence of northerlies identified by Figure 9, and the zonal average over 110 to 120°E is representative of the prominent front that spans across the rainband longitudes. The northerlies are stronger in the mid to upper troposphere, whereas the southerlies concentrate in the lower to mid-troposphere.

Rainband-composite anomalies of the seasonal (May to August) meridional wind over East China show the prominence of the northerlies north of 30°N (Figure 11), but not the southerlies. The sharp meridional gradient of the moist static energy also shows that the position of the front is around 30° N, indicating that the rainbands detected by our algorithm are indeed frontal precipitation. This anomaly pattern suggests that the northerlies are the critical triggers for the formation of the front, and of the rainband. Southerlies appear to also play a role, but prior to rainband formation. The bottom panel of Figure 11 shows the anomalous composite of V two days before the rainband events, indicating enhanced southerlies to the south of the rainband in the lower atmosphere. However, the front is only partially enhanced at this time, and the rainband has not yet formed completely. This suggests that while anomalous southerlies act to increase moisture over East Asia, it is the anomalous northerlies that act as the trigger for rainband formation.

The seasonal trajectory of the convergence zone also tracks the northward migration of the rainbands from spring to summer. Figure 12 (upper panel) shows agreement between the latitude of the rainband (blue line) and the latitude where the northerlies and southerlies converge (color contour), especially from May to July. In August, the climatological northerlies appear to be too far north or too weak; occasional episodes of strong, transient northerlies only appear concurrently with the East Asian rainbands throughout the rainband season, as shown in Figure 12 (middle panel). In June, the climatological northerlies are prominent, but in late July and August, the climatological northerlies are weaker, so in order to create a front, a much stronger anomalous northerly is needed, as shown in the third panel. Rainband events are also much less frequent in August. The role of the background northerly is hence important from May to July when the rainbands are the most frequent. The strongest northerly winds occur in May and June and become weaker in July and August, consistent with the fact that the upstream jet stream is weakening and progressing northward of the Tibetan Plateau, with weakening of the associated topographic Rossby waves. May has fewer rainband events than June, even though May sees slightly stronger northerly, due to less available moisture in May.

The northerly wind responsible for the convergence is a combination of a background (climatological) flow and a transient circulation, as shown in figure 12, where the climatology and anomaly of V exist together. We hypothesize that the background northerlies over East Asia consist in part of topographic Rossby waves forming downstream of the Tibetan Plateau. At 90°E, the longitude of the Tibetan Plateau, the jet stream is south of the Plateau ($<$28°N) in winter and north of the Plateau ($>$38°N) in August. At 75°E, upstream of the Tibetan Plateau, however, the maximum zonal wind at 500 hPa, $U_{500,max}$, stays around 30°N from December to April and starts moving north only in April (Figure 13 left panels). $U_{500,max}$ moves across the Tibetan Plateau from April to June and past its northern boundary mid-June. From mid-June to August, slower westerly winds still encounter the Tibetan Plateau even though the maximum wind speed is north of the topography.

The dynamics of westerly flow impinging on a mountain barrier is illustrated in Holton and Hakim (2013): with the conservation of potential vorticity, a fluid column moving eastward to cross a barrier acquires anticyclonic vorticity and moves southward downstream. This southward flow contributes to the northerly wind that is crucial to the formation of the rainbands. The northerly wind weakens and almost disappears in the summer because the upstream jet stream already has its maximum moving off the Tibetan Plateau, and the westerly wind is weak in general.

Figure 13 right panel shows a Hovmoller diagram of the 500 hPa meridional wind anomaly averaged between 36°N to 46°N, and compares the calculated downstream wavelength with the upstream 500 hPa westerly wind speed maximum $U_{500,max}$ and its latitude. The latitudinal range of 36°N to 46°N captures the maximum northerlies and facilitates the analysis of the longitudinal structure. At each time, the downstream V shows northerlies immediately to the east of the Tibetan Plateau and oscillations eastward. The wavelength of the oscillations is estimated roughly as the distance between two peaks, or double the distance between the northerlies immediately east of the Tibetan Plateau and the ensuing southerlies. The wavelengths shorten from April to August, co-incident with the summer weakening of the upstream westerlies between 28°N to 38°N. This is consistent with the variation of topographic Rossby wavelengths with upstream wind speed (Holton and Hakim (2013); Vallis (2017). We therefore hypothesize that variations in the amplitude and wavelengths of the topographic Rossby waves downstream of the Tibetan Plateau contribute to the northerlies that determine the northward migration of the rainbands. Notice that the northerly winds depicted here are the climatology, different from the rainband-event composites shown in Figure 11. It shows here that the background condition from May to August already favors northerlies, and the northerlies are even stronger when rainband events happen.

On top of the interaction with the Tibetan Plateau, the jet stream also has its maximum speed at the coast of Asia, and classic theory of ageostrophic circulation states that a front will be generated at the jet entrance region (see Holton and Hakim (2013)). A transverse circulation with an ascending branch to the south of the jet stream and a descending branch to the north of the jet stream in the height-latitude plane, similar to the Hadley cell, is then generated to provide acceleration to the upper-level zonal wind. In the ERA-Interim product, the transverse circulation is the strongest in May with ascending motion (red shading) south of the jet core and descending motion (blue shading) to the north (Figure 14). This pattern is less prominent in June, and even weaker in July and August, even though the East Asian rainband is the most frequent in June and July. While the diagnostic relationship of the ageostrophic flow still holds to some extent here, it appears to not be able to explain the peak rainband frequency in June and July. Also, the fundamental cause for the jet entrance and the intensified meridional temperature gradient to appear here might, in turn, be attributed to the meridional flow discussed in previous sections.

While the southward extent of the northerlies determine the latitudinal position of the fronts, the southerly winds provide warm moist air from the ocean, fueling the intense precipitation of the East Asian rainbands. The climatological column-integrated moisture transport in Figure 15 suggests that most water vapor over East Asia comes from three sources: the Bay of Bengal, the South China Sea, and the Western Pacific; Chiang et al. (2020) also confirmed these sources using trajectory analysis. In May and June, moisture from the Bay of Bengal travels eastward to Southeast Asia and China and Japan. The onset of this transport is an indicator of the onset of the East Asian summer monsoon (Ding and Chan (2005)). In July, this westerly moisture source significantly weakens, and the moisture from the South China Sea starts to dominate, as the subtropical high pressure system over the Pacific moves northward from May to August and steers the moisture from the South to the northwest to reach the coast of China, and in July to the northeast towards Japan. As a result of the two moisture sources, East Asia has ample moisture throughout these four months. The column integrated moisture convergence is strong in the Yangtze River Basin in May, and extends westward to align with the shape of the rainband in June. In July and August, the rainband is not the dominating signature of the moisture convergence.

Rainband-composite anomalies of moisture transport (Figure 16) show that much of the intense moisture transport into the rainbands comes from the Pacific. The contribution from the Bay of Bengal is minimal, suggesting the rainband is not fueled by moisture far west, but rather from the Pacific and potentially some local recycling. Also, moisture transport from afar will take time and is likely done before the precipitation, as suggested by the bottom panel of Figure 11. It is worth noting that the anomaly in the moisture transport collocates with the rainbands and is smaller than the climatological moisture transport, suggesting that a slight enhancement of southerly influx of warm and moist into the convergence.

5. Conclusion and Discussion

This study, for the first time, identifies individual East Asian rainband events from May to August and relates them to the large-scale circulation. A machine learning method is used to detect East Asian rainbands in the 6-hourly ERA-Interim reanalysis product for 1979-2018. The frequency of rainbands increases from May to a maximum in June, and decreases thereafter, consistent with previous studies using daily or pentad precipitation data. By contrast, a snapshot climatology of the 6-hourly rainband trajectory shows that their northward migration is steady and their median duration is 16 hours, suggesting that the interludes of slow migration or pauses are synoptic in nature and may occur only in some years. The length and the duration of the rainbands increase monotonically from May to June, but the intensity of the rainfall within rainbands shows a small dip in late May before it reaches its maximum in late June.

We find that the occurrences of rainband events are specifically tied to the occurrence of enhanced northerlies over East Asia. The climatological northerly wind together with the synoptic transient northerly wind contribute to the formation of the front for the rainbands. Part of the climatological northerly wind can be attributed to Rossby waves excited by the Tibetan Plateau from upstream westerly zonal winds. As the jet stream, the fastest core of this zonal wind, moves northward and off the Tibetan Plateau, the northerly wind over East Asia weakens and disappears in the summer, effectively ending the rainband season. The jet entrance region near East China would also facilitate updraft and hence convection, but the ageostrophic flow is the most prominent in May and not obvious in July and August. This is not to say that monsoonal southerlies are not important: they exist as a background flow that steadily supplies warm moist air from the ocean to the convergence zone and persist through the monsoon season (May to August). There is also suggestion of enhanced southerlies prior to rainband events. However, it is the enhanced northerlies that direct the actual formation of the rainband.

In this study, we have focused on the identification and characterization of the East Asian rainbands, followed by a discussion of the associated circulation pattern. Instead of the climatology of the East Asian Summer Monsoon that has been extensively studied before, this study demonstrates the possibility to investigate individual rainband events and to distinguish anomalous rainband-inducing flows from background conditions. We also discuss the possible dynamic effects that lead to the rainband-inducing flows. Circulation responses to thermodynamic and hydrodynamic forcing, such as heating over the plateau, are also important components of the complex South East Asian summer monsoon system, and contribute to setting the background circulation. Their role in the seasonal migration of the rainbands, however, has not been explored, and is beyond the scope of this study. The thermodynamic and hydrodynamic processes, as part of the background conditions, are important for precipitation amounts, whose variability depends, in addition, on sea surface temperature, local recycling and other processes that supply moisture, as well as on cloud microphysical processes and climate forcing. The linkage of the location of the frontal convergence zone to the latitudinal profile of westerlies upstream of the Tibetan Plateau, as found in this analysis, could provide an additional dimension to the projection of summer monsoon rainfall over East Asia.

Acknowledgments. This work was supported by National Science Foundation Grants EAR-0909195 and EAR-1211925 and Department of Energy Grant DE-SC0014078. We thank William R. Boos, Michael Wehner, and Burlen Loring for very helpful discussions and support. This research used resources of the National Energy Research Scientific Computing Center (NERSC), a U.S. Department of Energy Office of Science User Facility operated under Contract No. DE-AC02-05CH11231.

Data availability statement. All ERA-Interim Reanalysis data used in this study are available from the European Centre for Medium-Range Weather Forecasts (ECMWF) at `http://apps.ecmwf.int/datasets/data/interim-full806moda/` as cited in Dee et al. (2011). The derived data and calculation results of the East Asian rainbands in this work have been archived and are available at `https://doi.org/10.6078/D1GQ5R`.

References

Barrett, A. I., S. L. Gray, D. J. Kirshbaum, N. M. Roberts, D. M. Schultz, and J. G. Fairman Jr, 2015: Synoptic versus orographic control on stationary convective banding. *Quarterly Journal of the Royal Meteorological Society*, **141 (689)**, 1101–1113.

Chang, E. K., 2009: Diabatic and orographic forcing of northern winter stationary waves and storm tracks. *Journal of climate*, **22 (3)**, 670–688.

Chen, B., J. Yang, and J. Pu, 2013: Statistical characteristics of raindrop size distribution in the meiyu season observed in eastern china. *Journal of the Meteorological Society of Japan. Ser. II*, **91 (2)**, 215–227.

Chiang, J. C., M. J. Herman, K. Yoshimura, and I. Y. Fung, 2020: Enriched east asian oxygen isotope of precipitation indicates reduced summer seasonality in regional climate and westerlies. *Proceedings of the National Academy of Sciences*.

Day, J. A., I. Fung, and W. Liu, 2018: Changing character of rainfall in eastern china, 1951–2007. *Proceedings of the National Academy of Sciences*, **115 (9)**, 2016–2021.

Day, J. A., I. Fung, and C. Risi, 2015: Coupling of south and east asian monsoon precipitation in july–august. *Journal of Climate*, **28 (11)**, 4330–4356.

Dee, D. P., and Coauthors, 2011: The era-interim reanalysis: Configuration and performance of the data assimilation system. *Quarterly Journal of the royal meteorological society*, **137 (656)**, 553–597.

Ding, Y., and J. C. Chan, 2005: The east asian summer monsoon: an overview. *Meteorology and Atmospheric Physics*, **89 (1-4)**, 117–142.

Fairman, J. G., D. M. Schultz, D. J. Kirshbaum, S. L. Gray, and A. I. Barrett, 2016: Climatology of banded precipitation over the contiguous united states. *Monthly Weather Review*, **144**, 4553–4568.

Hagen, M., 1992: On the appearance of a cold front with a narrow rainband in the vicinity of the alps. *Meteorology and Atmospheric Physics*, **48 (1-4)**, 231–248.

He, L., Y. Chao, K. Suzuki, and K. Wu, 2009: Fast connected-component labeling. *Pattern recognition*, **42 (9)**, 1977–1987.

Held, I. M., M. Ting, and H. Wang, 2002: Northern winter stationary waves: Theory and modeling. *Journal of climate*, **15 (16)**, 2125–2144.

Holton, J., and G. Hakim, 2013: *An introduction to dynamic meteorology. Waltham, MA*. Academic Press.

Houze, R. A., P. V. Hobbs, K. R. Biswas, and W. M. Davis, 1976: Mesoscale rainbands in extratropical cyclones. *Monthly Weather Review*, **104 (7)**, 868–878.

Kong, W., and J. C. Chiang, 2020: Interaction of the westerlies with the tibetan plateau in determining the mei-yu termination. *Journal of Climate*, **33 (1)**, 339–363.

Lau, K., M. Kim, and K. Kim, 2006: Asian summer monsoon anomalies induced by aerosol direct forcing: the role of the tibetan plateau. *Climate dynamics*, **26 (7-8)**, 855–864.

Liang, P., and J. He, 2008: Review for climate change of meiyu over the yangtze-huaihe basins. *Plateau Meteorol*, **27**, 1–15.

Liang, X.-Z., and W.-C. Wang, 1998: Associations between china monsoon rainfall and tropospheric jets. *Quarterly Journal of the Royal Meteorological Society*, **124 (552)**, 2597–2623.

Matsumura, S., T. Horinouchi, S. Sugimoto, and T. Sato, 2016: Response of the baiu rainband to northwest pacific sst anomalies and its impact on atmospheric circulation. *Journal of Climate*, **29 (8)**, 3075–3093.

Molnar, P., W. R. Boos, and D. S. Battisti, 2010: Orographic controls on climate and paleoclimate of asia: thermal and mechanical roles for the tibetan plateau. *Annual Review of Earth and Planetary Sciences*, **38**.

Ninomiya, K., and H. Muraki, 1986: Large-scale circulations over east asia during baiu period of 1979. *Journal of the Meteorological Society of Japan. Ser. II*, **64 (3)**, 409–429.

Niziol, T. A., W. R. Snyder, and J. S. Waldstreicher, 1995: Winter weather forecasting throughout the eastern united states. part iv: Lake effect snow. *Weather and Forecasting*, **10 (1)**, 61–77.

Roe, G. H., 2005: Orographic precipitation. *Annu. Rev. Earth Planet. Sci.*, **33**, 645–671.

Sampe, T., and S.-P. Xie, 2010: Large-scale dynamics of the meiyu-baiu rainband: Environmental forcing by the westerly jet. *Journal of Climate*, **23 (1)**, 113–134.

Son, J.-H., K.-H. Seo, and B. Wang, 2019: Dynamical control of the tibetan plateau on the east asian summer monsoon. *Geophysical Research Letters*, **46 (13)**, 7672–7679.

Son, J.-H., K.-H. Seo, and B. Wang, 2020: How does the tibetan plateau dynamically affect downstream monsoon precipitation? *Geophysical Research Letters*, **47 (23)**, e2020GL090 543.

Sun, Q., C. Miao, Q. Duan, H. Ashouri, S. Sorooshian, and K.-L. Hsu, 2018: A review of global precipitation data sets: Data sources, estimation, and intercomparisons. *Reviews of Geophysics*, **56 (1)**, 79–107.

Vallis, G. K., 2017: *Atmospheric and oceanic fluid dynamics*. Cambridge University Press.

Wang, B., 2002: Rainy season of the asian–pacific summer monsoon. *Journal of Climate*, **15 (4)**, 386–398.

Wang, B., and T. Li, 2004: East asian monsoon-enso interactions. *East Asian Monsoon*, World Scientific, 177–212.

Wu, C.-H., M.-D. Chou, and Y.-H. Fong, 2018: Impact of the himalayas on the meiyu–baiu migration. *Climate dynamics*, **50 (3-4)**, 1307–1319.

Wu, G., and Coauthors, 2015: Tibetan plateau climate dynamics: recent research progress and outlook. *National Science Review*, **2 (1)**, 100–116.

Xu, H., J. He, and B. Zhou, 2001: The features of atmospheric circulation during meiyu onset and possible mechanisms for westward extension (northward shift) of pacific subtropical high. *Quart. J. Appl. Meteor*, **12**, 150–158.

Yoshizaki, M., and Coauthors, 2000: Analytical and numerical study of the 26 june 1998 orographic rainband observed in western kyushu, japan. *Journal of the Meteorological Society of Japan. Ser. II*, **78 (6)**, 835–856.

Zhou, Y., S. Gao, and S. S. Shen, 2004: A diagnostic study of formation and structures of the meiyu front system over east asia. *Journal of the Meteorological Society of Japan. Ser. II*, **82 (6)**, 1565–1576.

LIST OF FIGURES

Fig. 1. Flow chart of the machine learning method to identify individual East Asian rainband. The full dataset of the 6-hourly total precipitation over East Asia from 1979 to 2018 is used. The potential rainband candidates are selected based on the initial thresholds of 10 mm/day and 10° longitude long. A small subset (approximately 20%) of the potential rainband candidates are manually reviewed to identify narrow bands. A convolutional neural network is then trained to identify rainbands in the remainder of the dataset. 32

Fig. 2. An example of the true positive (a) and a false positive (b) in the rainband detection algorithm. The red and green contours show the total precipitation of 10 and 15 mm/day, respectively. Both have precipitation features that extend more than 10^o in longitude. Precipitation over East China and Western Pacific in (a) forms a narrow band and is identified as a rainband, while the precipitation in (b) is unorganized and does not form a long and narrow band, so will not be identified as a rainband. 33

Fig. 3. Snapshot climatology of the latitude and the length of the East Asian rainbands from May to August over 1979 to 2018, showing the latitude of the centroids of rainbands (y-axis) and the length of each rainband (color). The domain is 20-45°N and 110-145°E. Each data point represents 40-year average at that 6-hour window of the year, and there are $4 \times 31 \times 40$ points in the May average, for example. The dark blue line is the 30-day smoothed plot of the centroid latitude of the rainbands. May to August is the peak season for long rainbands over East Asia, and the rainbands migrate north from May to the end of July, and then are largely dispersed while migrating south in August. 34

Fig. 4. Climatology of the east-west extent of the rainbands from May to August. The solid blue lines show the climatological eastern boundary (upper) and western boundary (lower) of the rainbands; the dashed black line shows the climatological length of the rainbands in degrees longitude. The length of the rainbands grows from May to June, starts to decrease in late June, and stabilizes in August. The rainbands first stretch their eastern boundary in May from 132°E to 136°E, and then extend their western boundary in June from 120°E to 115°E. In July, the western boundary retreats to 120°E. 35

Fig. 5. Rainband-composite of total precipitation for each month from May to August. All 40 years (1979-2018) are considered, and 503 rainbands are detected in May, 1047 rainbands in June, 473 rainbands in July, and 166 rainbands in August. With 40 years of records and 4 snapshots per day, the numbers translate to 3.1 days in May, 6.5 days in June, 3.0 days in July, and 1.0 days in August with rainbands on average. The red contour denotes 10 mm/day. 36

Fig. 6. Rainband-composite anomalies of precipitation for each month from May to August. All 40 years (1979-2018) are included, similar to Figure 5. The red contour shows 5 mm/day as the difference between the rainband-composite and the monthly mean. 37

Fig. 7. Climatology of the average intensity (y-axis) and the size (color) of the rainbands. The average intensity is defined as the total amount of rain in each rainband divided by the number of grid points in the rainband. The size is defined as the number of grid points, and is the approximately areal coverage of the rainbands. The intensity of the rainbands increases a little during May and drops back down, before it picks up again in June and drops again from late June to late July. Then it stabilizes in August before it slightly increases in late August. The size of the rainband increases from May to June and stabilizes, before it maximizes in the first half of August. The size trend and the length trend (Figure 4) together mean that the rainbands are more spread out in the north-south direction from late June to August. 38

Fig. 8. Distribution of the duration of the rainband events for each month. Duration is calculated as the number of continuous snapshots in which a rainband is detected, multiplied by the time interval between two snapshots (6 hours). The shortest rainband events are only in 1 snapshot, possibly shorter than 6 hours but assumed to be 6 hours here. The longest rainband event lasted 228 hours in June 1998. 39

Fig. 9. Rainband-composites (left column) and monthly means (right column) of 500 hPa wind vectors from May to August. A strong northerly component in the wind over East China is seen in all four months. The monthly mean wind also has a prominent northerly component in May and June, but not in July and August. 40

Fig. 10. Rainband-composite anomalies of the 500 hPa wind, i.e. the difference between the left and the right columns in Figure 9. A northerly wind anomaly is prominent in all four months over East China when the rainbands are present. June has the weakest anomalous flow among the four months because the monthly-averaged wind in June already shows a strong cyclonic signature over East China (northerly) and Japan (southerly). The grey contour shows an outline of the Tibetan Plateau at 4000 m altitude. The color shading shows the moist static energy anomaly, namely the composite of MSE on rainband days minus the monthly mean MSE. 41

Fig. 11. Climatology (top) and rainband-composite anomalies and (middle) of the May-August meridional wind (arrows) averaged over 110°E and 120°E and the meridional gradient of moist static energy (color) averaged over 110°E and 120°E; (bottom) the same as the middle panel, but with V composited with a 2-day lag before the rainband events. Northerly winds north of 30°N are prominent in the rainband-composite anomalies, as is the sharp gradient of the moist static energy. Rainband-anomalies of southerly wind to the south of the front are largely absent, as are other features in the gradient of the moist static energy. 42

Fig. 12. Climatology (top), rainband-composite (middle) and rainband-composite anomalies (bottom) of meridional wind at 500 mb over 110°E and 120°E (color) and the latitude of the rainband centroid (blue line in top panel). The data is averaged daily. The latitude of the rainband is co-located with the latitude where the meridional wind approaches 0, suggesting the frontal rainband occurs where there is convergence of the meridional winds. The northerly wind north of the front persists from May to July but is weak or further north in August. 43

Fig. 13. Climatology of the zonal component of the upstream subtropical jet (U) and downstream meridional wind (V) of the Tibetan Plateau. The left two panels describe the maximum zonal wind speed and its latitude of the subtropical jet at 500 hPa averaged between 60°E to 75°E. The third panel is the downstream wavelength to the east of the Tibetan Plateau determined from the Hovemoller diagram of the meridional wind downstream of the Tibetan Plateau averaged between 36°N to 46°N (rightmost panel). The latitude and longitude ranges of the Tibetan Plateau(28°N to 38°N) are marked by dashed lines in the second and fourth panels, respectively. The solid white line in the fourth panel marks the longitude of the coastline. . . . 44

Fig. 14. Pressure-latitude cross-section of the pressure velocity ω (color shading) and the zonal wind U (black contour, unit is m/s). The green bar at the bottom of each subplot shows the latitudinal range of the East Asian rainband anomaly (5 mm/day) in each month. The longitudinal range of the domain is 110°E to 120°E. The ageostrophic flow, with updraft (red) south of the jet core and subsidence (blue) to the north, is prominent in May, but not obvious in July and August. 45

Fig. 15. The climatological column-integrated moisture transport (quiver) and the vertical integral of moisture convergence from May to August (1979-2018). Most water vapor over East Asia comes from three sources: the Bay of Bengal, the South China Sea, and the Western Pacific. In May, strong moisture convergence appears in the Yangtze River Basin in East China; in June, the moisture convergence extends westward to Japan, and the rainband signature dominates the monthly mean. In July and August, the rainband is not the most dominating feature of precipitation in East Asia; precipitation in the south takes over. 46

Fig. 16. Rainband-anomalies of the vertically-integrated moisture transport and of the moisture convergence from May to August (1979-2018). The anomalies are defined as the departure of the average moisture transport during rainband events from the average moisture transport of each month. 47

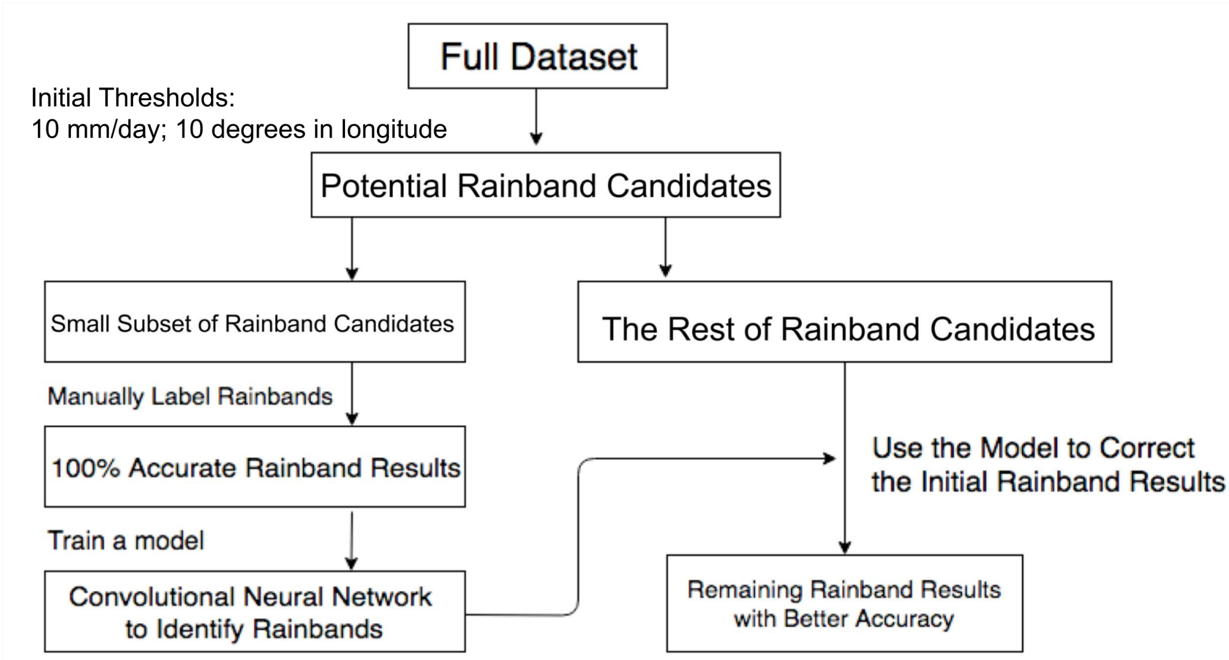

FIG. 1. Flow chart of the machine learning method to identify individual East Asian rainband. The full dataset of the 6-hourly total precipitation over East Asia from 1979 to 2018 is used. The potential rainband candidates are selected based on the initial thresholds of 10 mm/day and 10° longitude long. A small subset (approximately 20%) of the potential rainband candidates are manually reviewed to identify narrow bands. A convolutional neural network is then trained to identify rainbands in the remainder of the dataset.

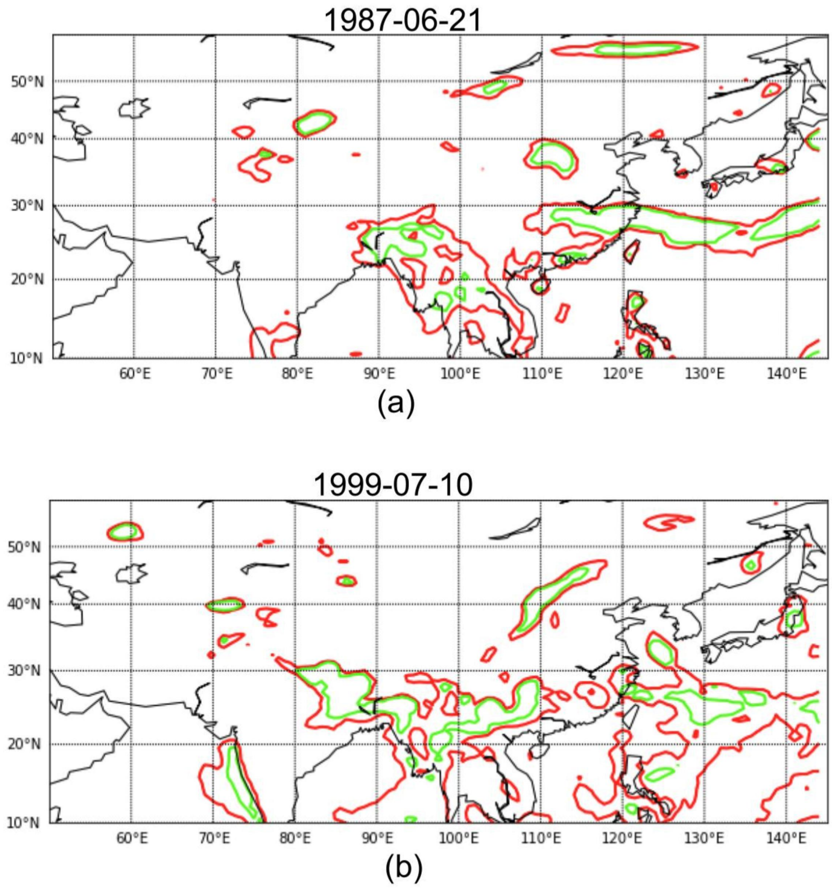

FIG. 2. An example of the true positive (a) and a false positive (b) in the rainband detection algorithm. The red and green contours show the total precipitation of 10 and 15 mm/day, respectively. Both have precipitation features that extend more than 10^o in longitude. Precipitation over East China and Western Pacific in (a) forms a narrow band and is identified as a rainband, while the precipitation in (b) is unorganized and does not form a long and narrow band, so will not be identified as a rainband.

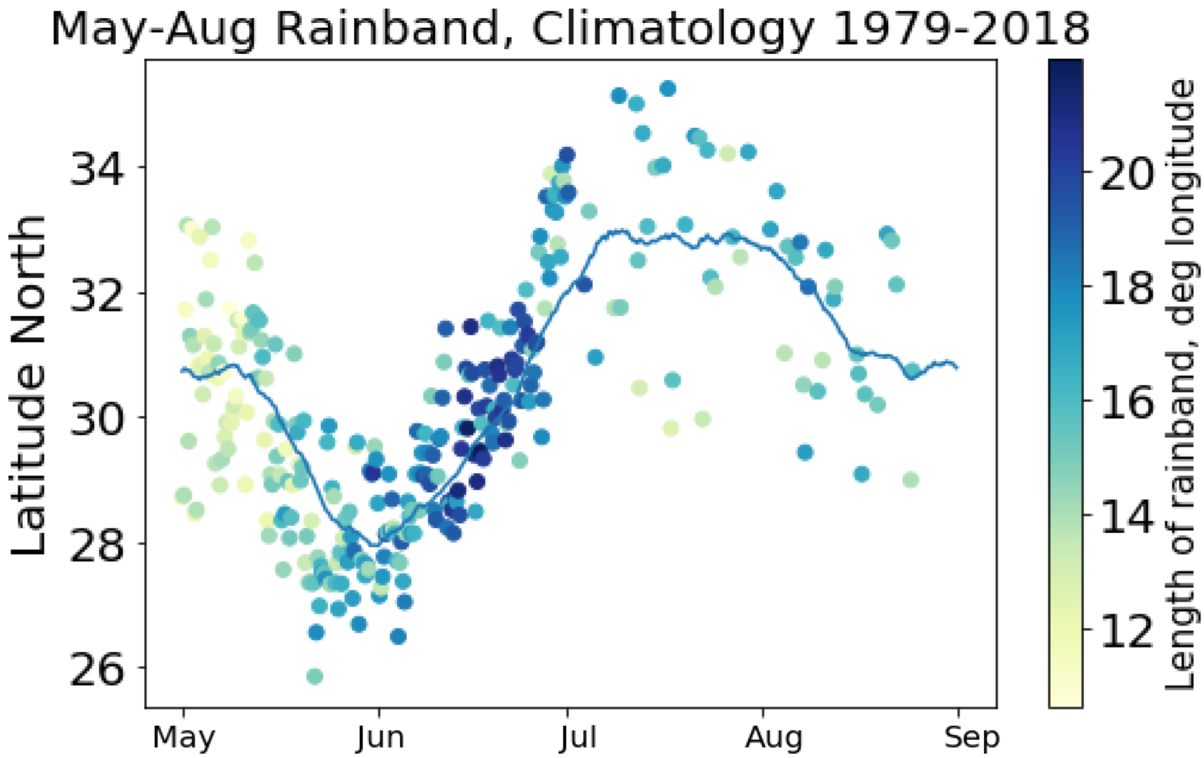

721 FIG. 3. Snapshot climatology of the latitude and the length of the East Asian rainbands from May to August over 1979 to 2018, showing the latitude of the centroids of rainbands (y-axis) and the length of each rainband (color). The domain is 20-45°N and 110-145°E. Each data point represents 40-year average at that 6-hour window of the year, and there are 4 × 31 × 40 points in the May average, for example. The dark blue line is the 30-day smoothed plot of the centroid latitude of the rainbands. May to August is the peak season for long rainbands over East Asia, and the rainbands migrate north from May to the end of July, and then are largely dispersed while migrating south in August.

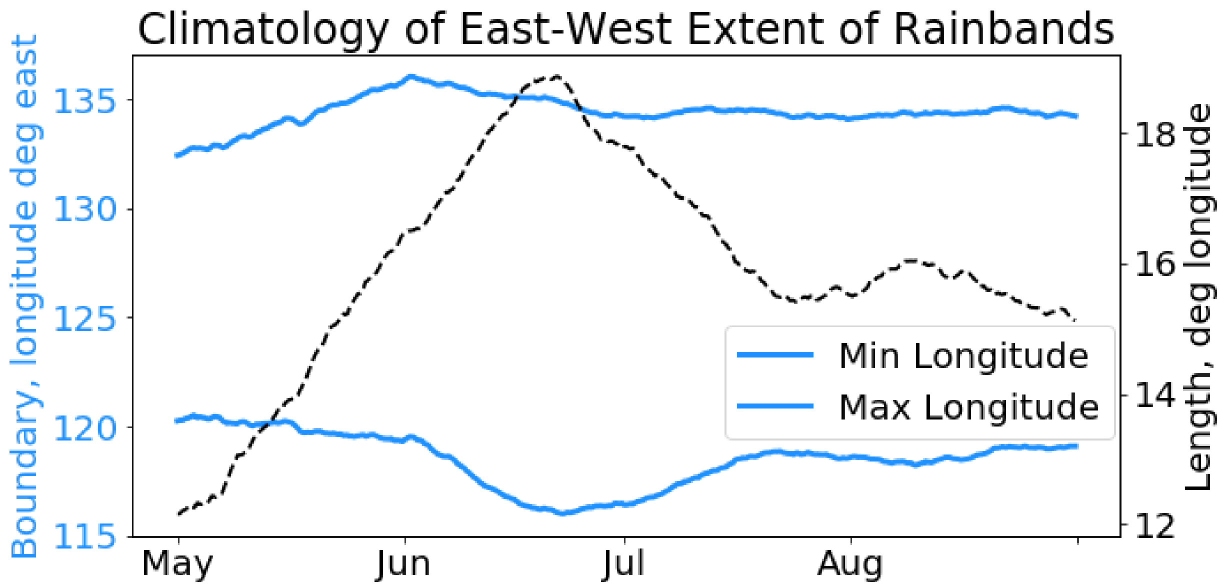

FIG. 4. Climatology of the east-west extent of the rainbands from May to August. The solid blue lines show the climatological eastern boundary (upper) and western boundary (lower) of the rainbands; the dashed black line shows the climatological length of the rainbands in degrees longitude. The length of the rainbands grows from May to June, starts to decrease in late June, and stabilizes in August. The rainbands first stretch their eastern boundary in May from 132°E to 136°E, and then extend their western boundary in June from 120°E to 115°E. In July, the western boundary retreats to 120°E.

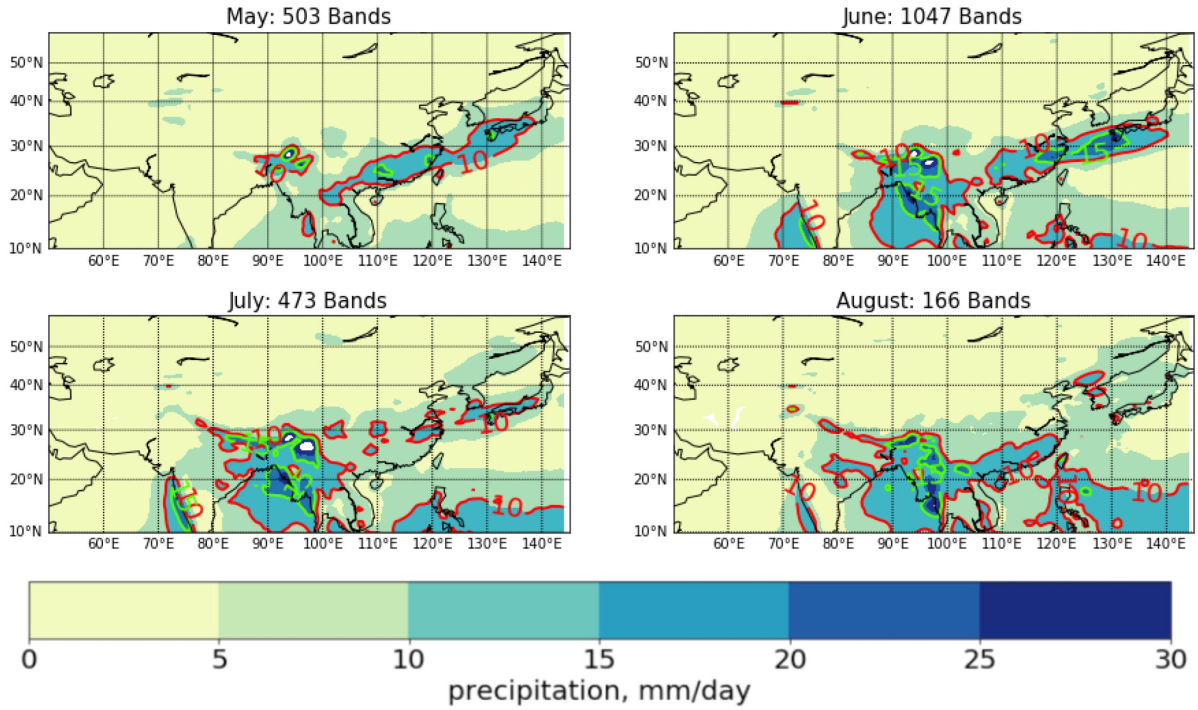

734 FIG. 5. Rainband-composite of total precipitation for each month from May to August. All 40 years (1979-2018) are considered, and 503 rainbands are detected in May, 1047 rainbands in June, 473 rainbands in July, and 166 rainbands in August. With 40 years of records and 4 snapshots per day, the numbers translate to 3.1 days in May, 6.5 days in June, 3.0 days in July, and 1.0 days in August with rainbands on average. The red contour denotes 10 mm/day.

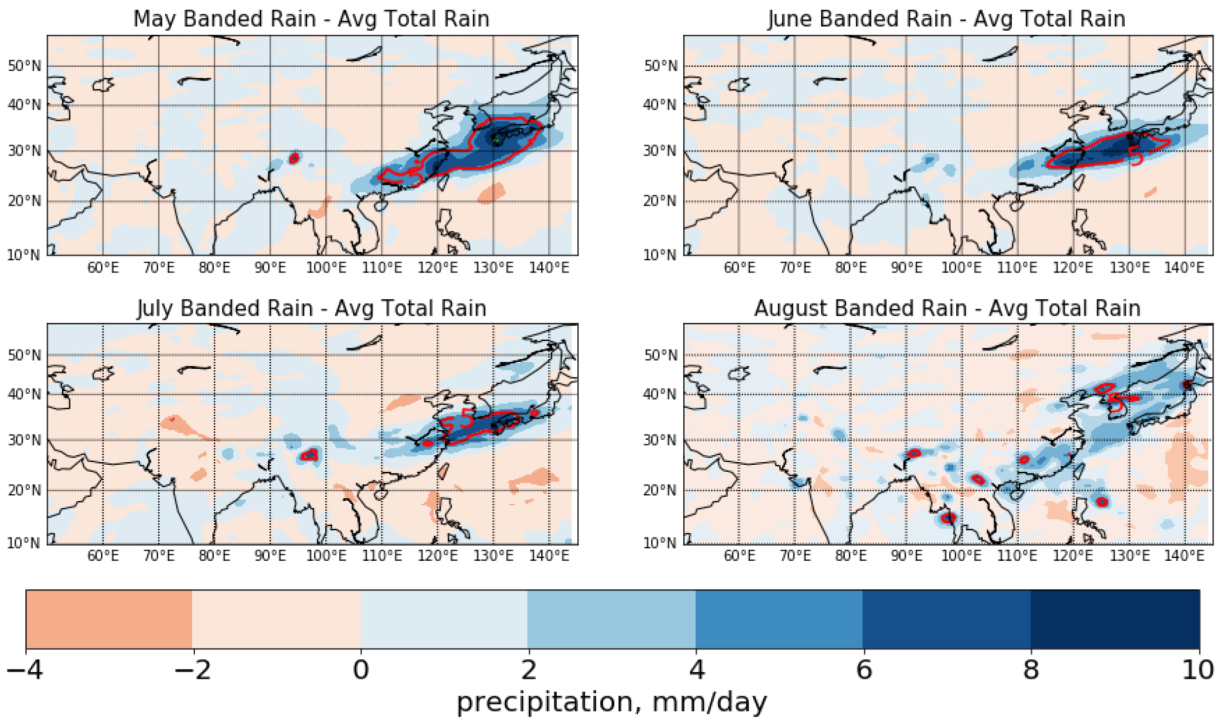

FIG. 6. Rainband-composite anomalies of precipitation for each month from May to August. All 40 years (1979-2018) are included, similar to Figure 5. The red contour shows 5 mm/day as the difference between the rainband-composite and the monthly mean.

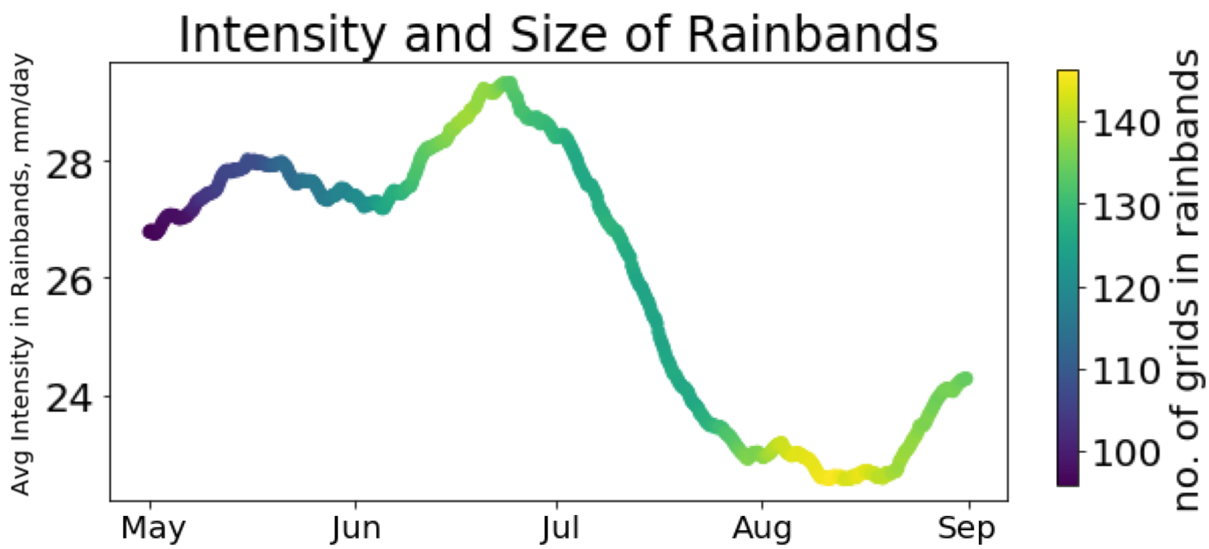

FIG. 7. Climatology of the average intensity (y-axis) and the size (color) of the rainbands. The average intensity is defined as the total amount of rain in each rainband divided by the number of grid points in the rainband. The size is defined as the number of grid points, and is the approximately areal coverage of the rainbands. The intensity of the rainbands increases a little during May and drops back down, before it picks up again in June and drops again from late June to late July. Then it stabilizes in August before it slightly increases in late August. The size of the rainband increases from May to June and stabilizes, before it maximizes in the first half of August. The size trend and the length trend (Figure 4) together mean that the rainbands are more spread out in the north-south direction from late June to August.

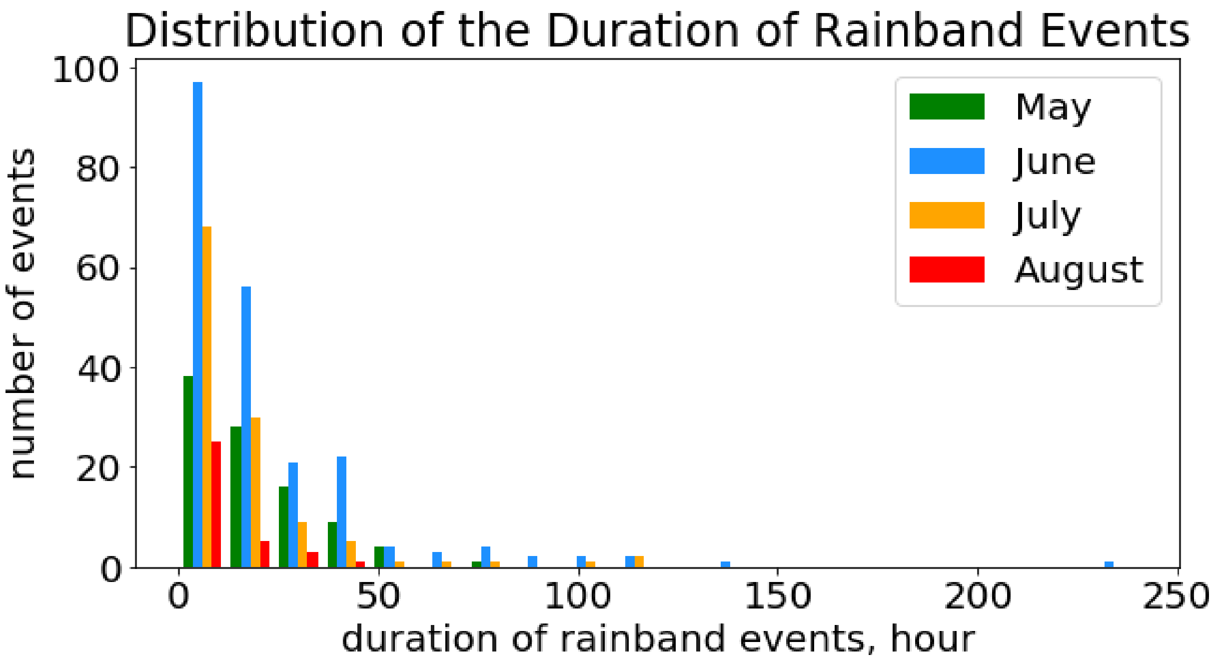

FIG. 8. Distribution of the duration of the rainband events for each month. Duration is calculated as the number of continuous snapshots in which a rainband is detected, multiplied by the time interval between two snapshots (6 hours). The shortest rainband events are only in 1 snapshot, possibly shorter than 6 hours but assumed to be 6 hours here. The longest rainband event lasted 228 hours in June 1998.

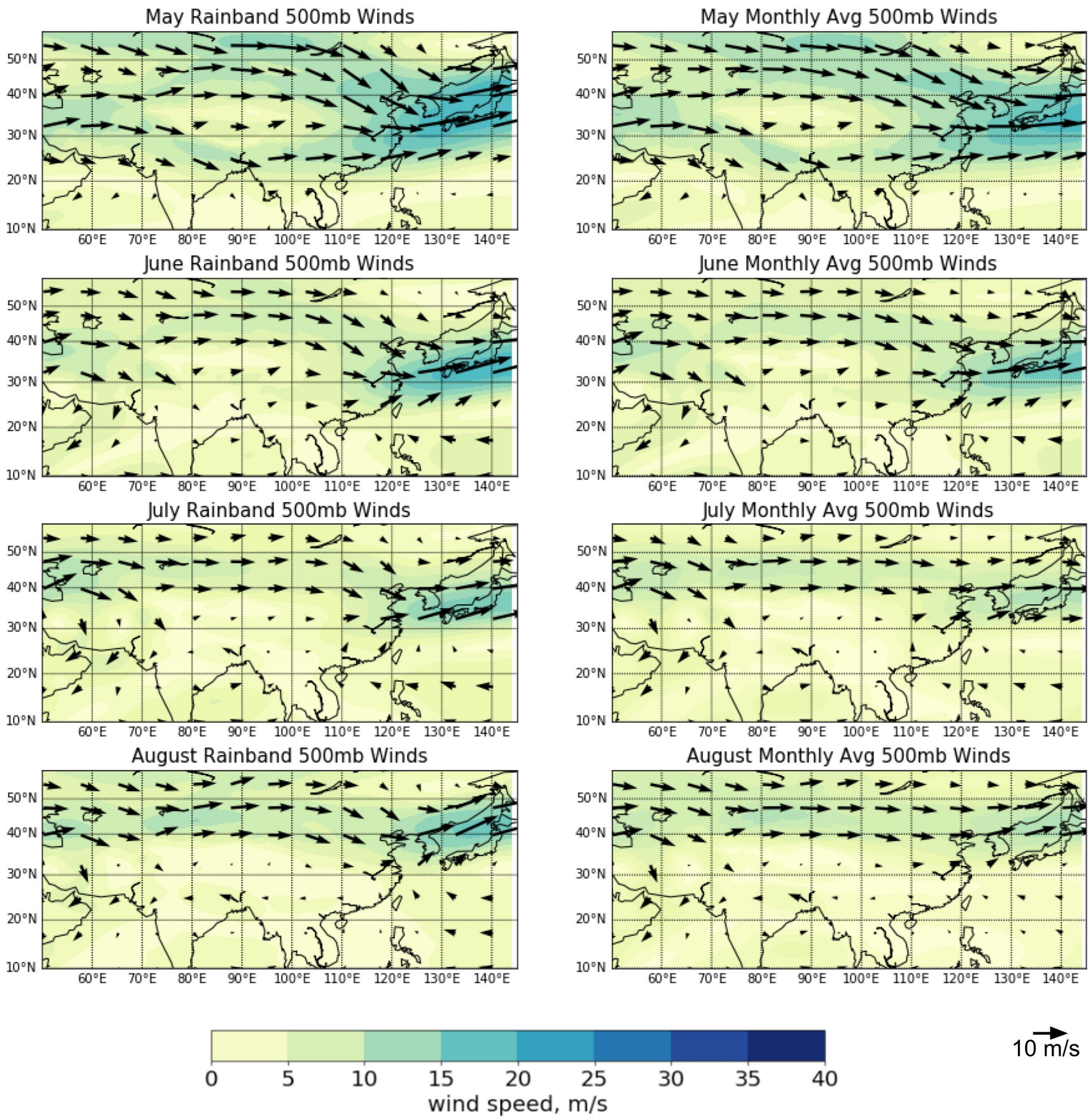

754 FIG. 9. Rainband-composites (left column) and monthly means (right column) of 500 hPa wind vectors from May to August. A strong northerly component in the wind over East China is seen in all four months. The monthly mean wind also has a prominent northerly component in May and June, but not in July and August.

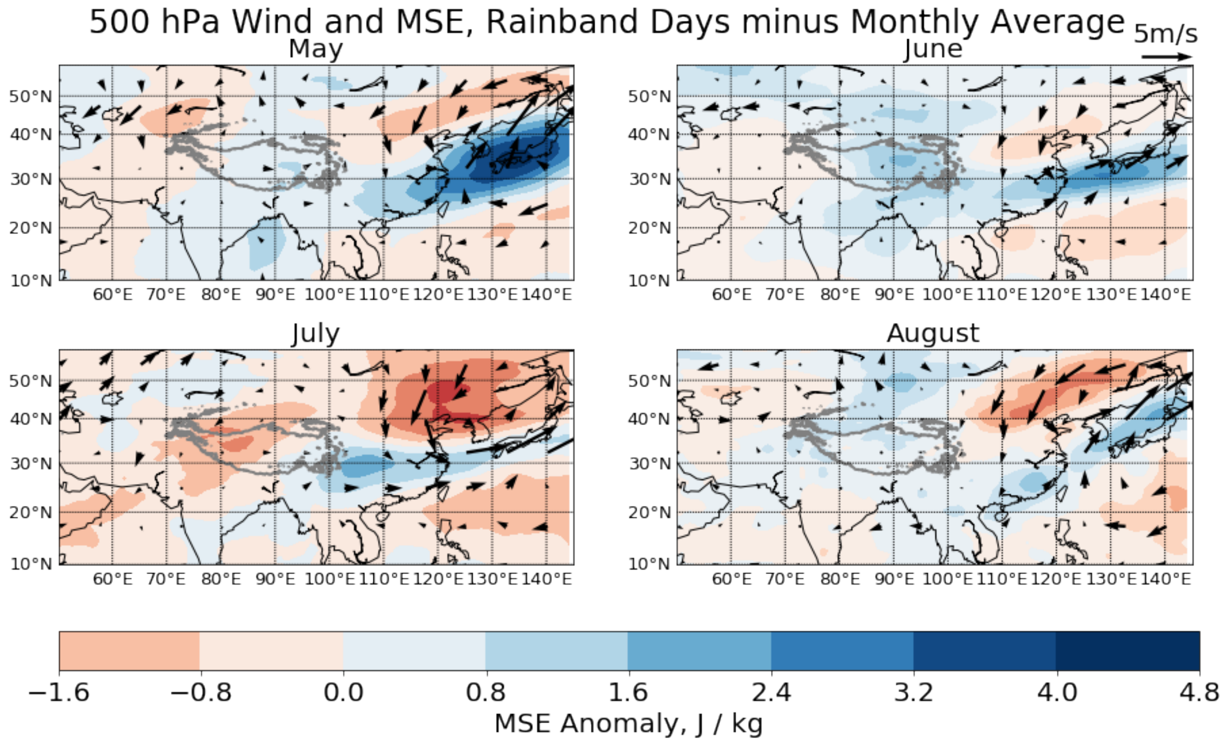

FIG. 10. Rainband-composite anomalies of the 500 hPa wind, i.e. the difference between the left and the right columns in Figure 9. A northerly wind anomaly is prominent in all four months over East China when the rainbands are present. June has the weakest anomalous flow among the four months because the monthly-averaged wind in June already shows a strong cyclonic signature over East China (northerly) and Japan (southerly). The grey contour shows an outline of the Tibetan Plateau at 4000 m altitude. The color shading shows the moist static energy anomaly, namely the composite of MSE on rainband days minus the monthly mean MSE.

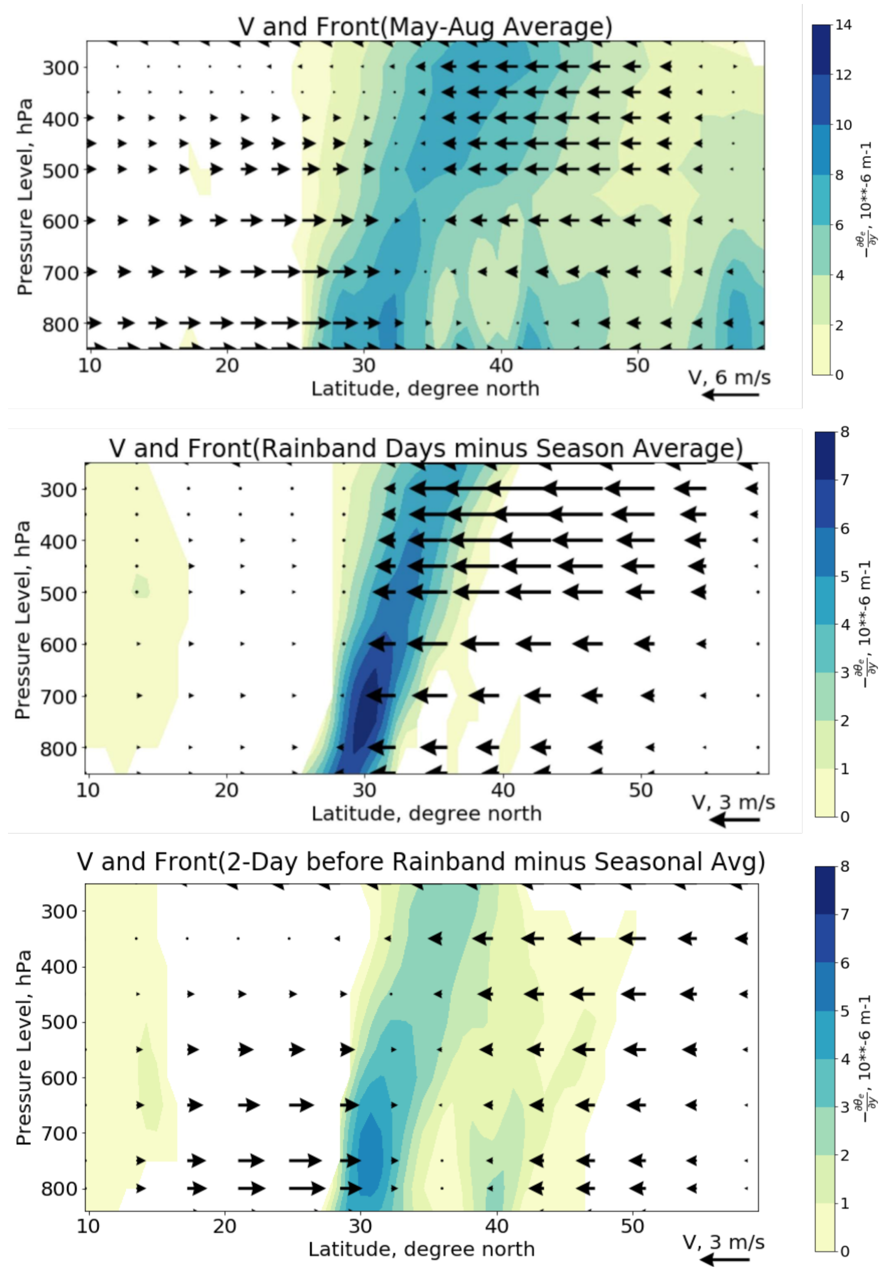

FIG. 11. Climatology (top) and rainband-composite anomalies and (middle) of the May-August meridional wind (arrows) averaged over 110°E and 120°E and the meridional gradient of moist static energy (color) averaged over 110°E and 120°E; (bottom) the same as the middle panel, but with V composited with a 2-day lag before the rainband events. Northerly winds north of 30°N are prominent in the rainband-composite anomalies, as is the sharp gradient of the moist static energy. Rainband-anomalies of southerly wind to the south of the front are largely absent, as are other features in the gradient of the moist static energy.

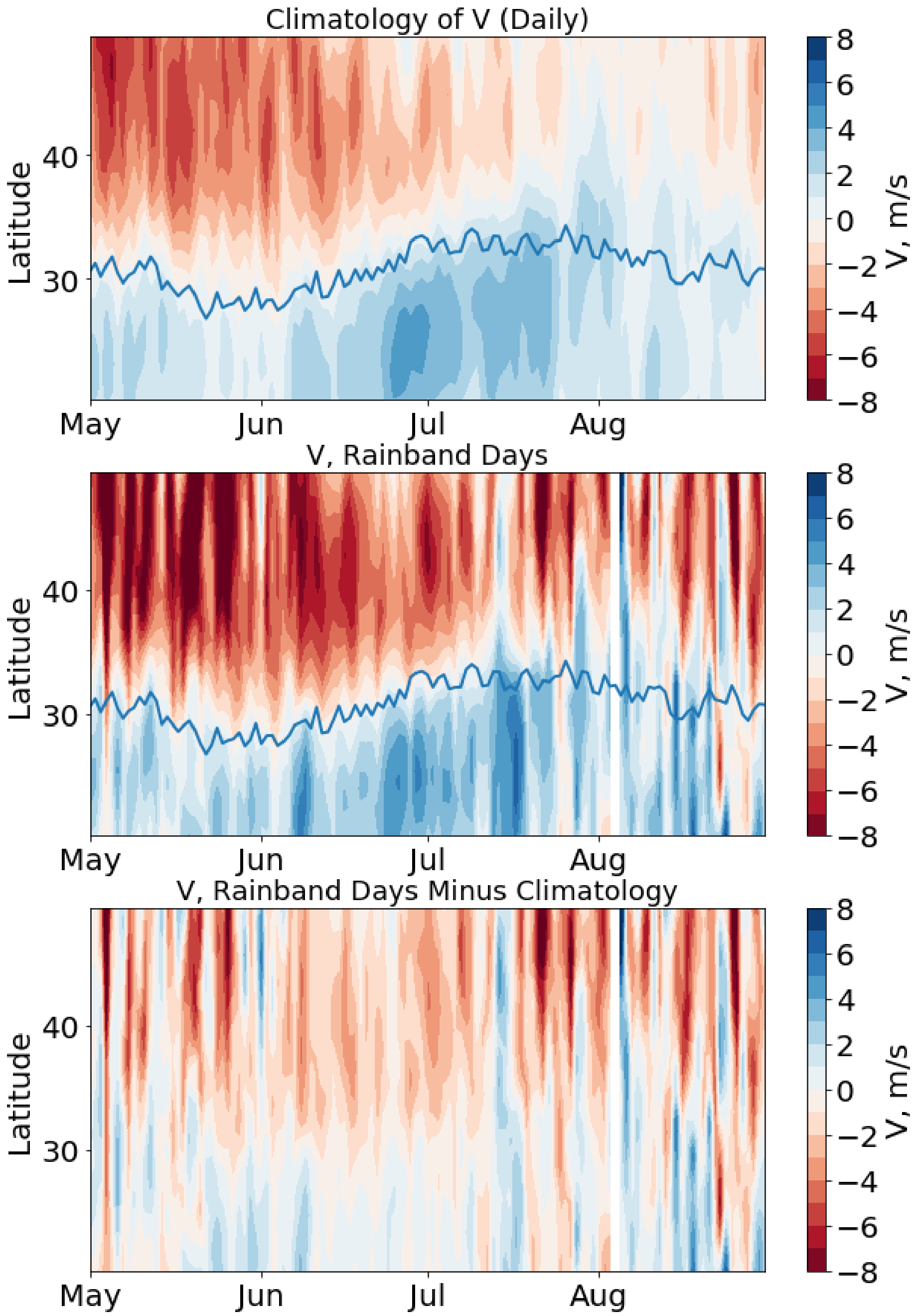

FIG. 12. Climatology (top), rainband-composite (middle) and rainband-composite anomalies (bottom) of meridional wind at 500 mb over 110°E and 120°E (color) and the latitude of the rainband centroid (blue line in top panel). The data is averaged daily. The latitude of the rainband is co-located with the latitude where the meridional wind approaches 0, suggesting the frontal rainband occurs where there is convergence of the meridional winds. The northerly wind north of the front persists from May to July but is weak or further north in August.

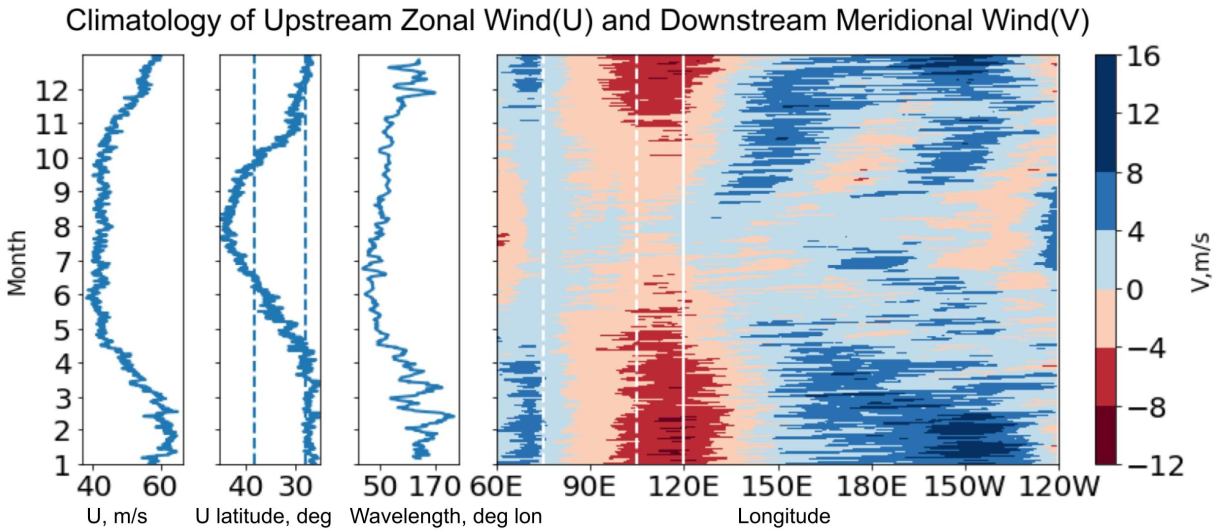

775 FIG. 13. Climatology of the zonal component of the upstream subtropical jet (U) and downstream meridional
776 wind (V) of the Tibetan Plateau. The left two panels describe the maximum zonal wind speed and its latitude of
777 the subtropical jet at 500 hPa averaged between 60°E to 75°E. The third panel is the downstream wavelength to
778 the east of the Tibetan Plateau determined from the Hovemoller diagram of the meridional wind downstream of
779 the Tibetan Plateau averaged between 36°N to 46°N (rightmost panel). The latitude and longitude ranges of the
780 Tibetan Plateau(28°N to 38°N) are marked by dashed lines in the second and fourth panels, respectively. The
781 solid white line in the fourth panel marks the longitude of the coastline.

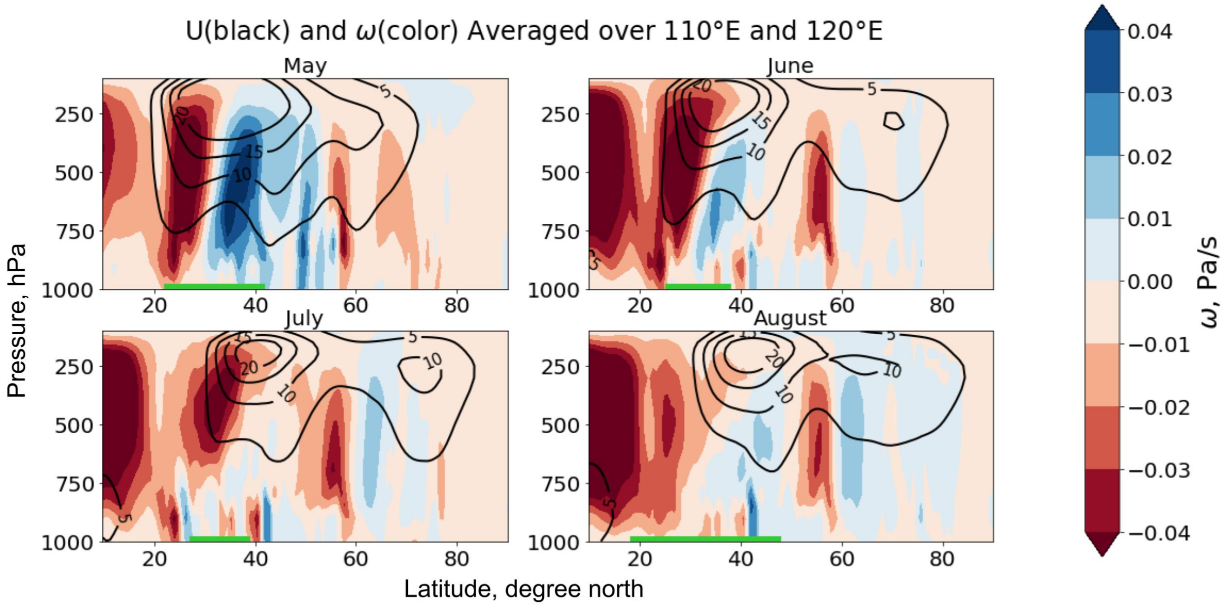

FIG. 14. Pressure-latitude cross-section of the pressure velocity ω (color shading) and the zonal wind U (black contour, unit is m/s). The green bar at the bottom of each subplot shows the latitudinal range of the East Asian rainband anomaly (5 mm/day) in each month. The longitudinal range of the domain is 110°E to 120°E. The ageostrophic flow, with updraft (red) south of the jet core and subsidence (blue) to the north, is prominent in May, but not obvious in July and August.

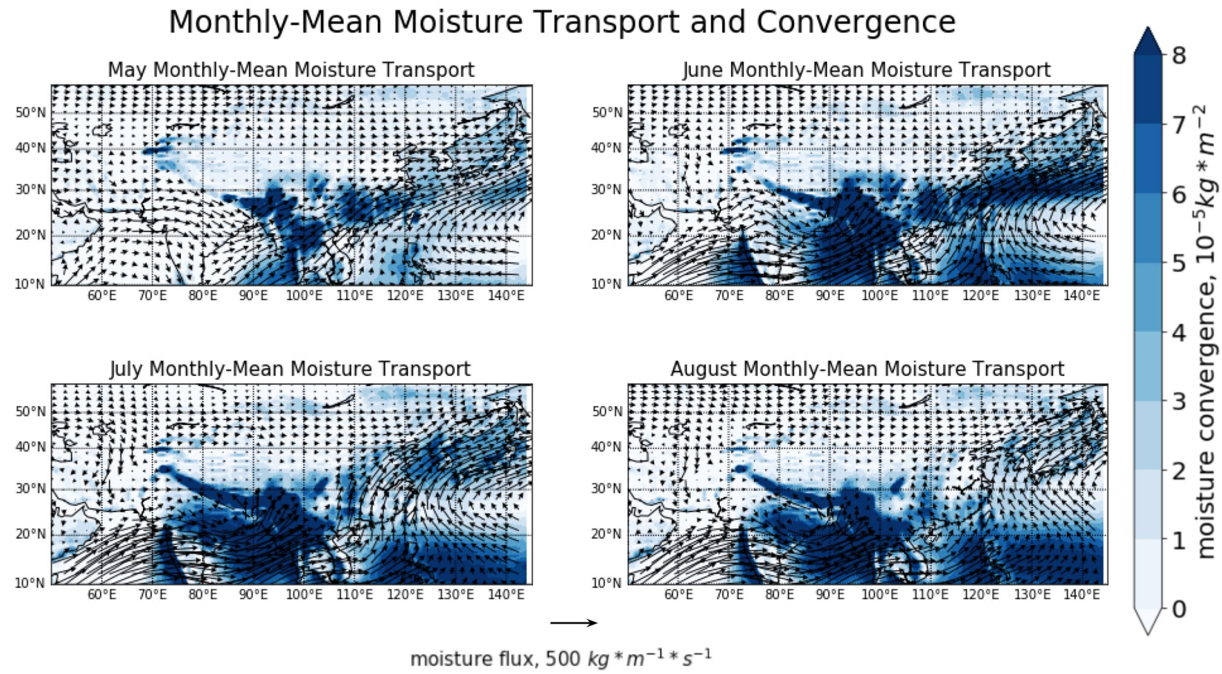

FIG. 15. The climatological column-integrated moisture transport (quiver) and the vertical integral of moisture convergence from May to August (1979-2018). Most water vapor over East Asia comes from three sources: the Bay of Bengal, the South China Sea, and the Western Pacific. In May, strong moisture convergence appears in the Yangtze River Basin in East China; in June, the moisture convergence extends westward to Japan, and the rainband signature dominates the monthly mean. In July and August, the rainband is not the most dominating feature of precipitation in East Asia; precipitation in the south takes over.

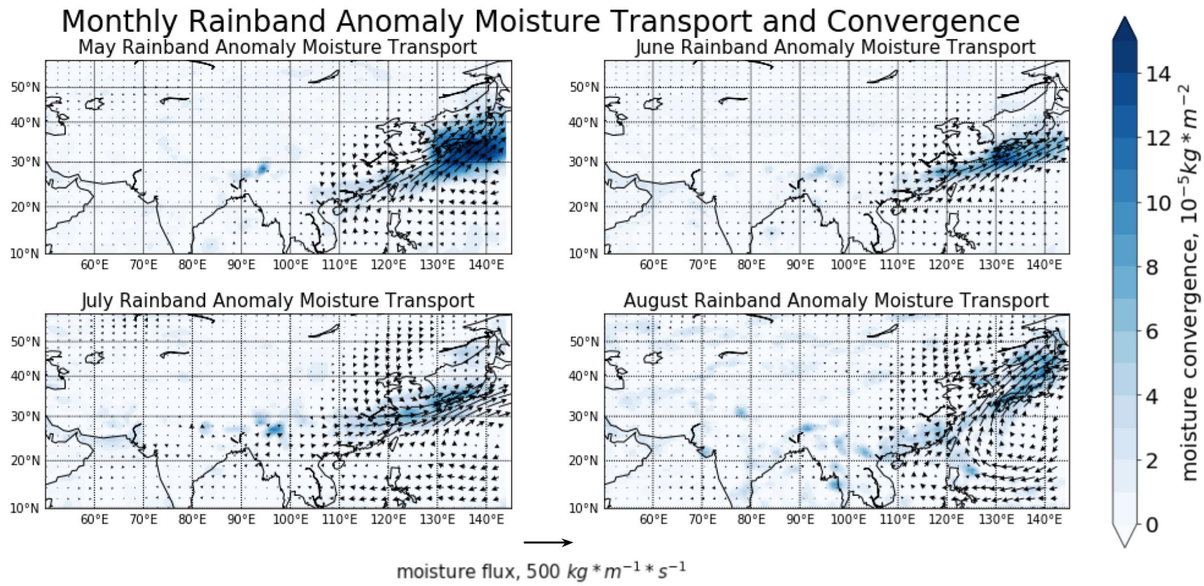

FIG. 16. Rainband-anomalies of the vertically-integrated moisture transport and of the moisture convergence from May to August (1979-2018). The anomalies are defined as the departure of the average moisture transport during rainband events from the average moisture transport of each month.